



PCCP

**Single-Photoelectron Collection Efficiency in 4D Ultrafast
Electron Microscopy**

Journal:	<i>Physical Chemistry Chemical Physics</i>
Manuscript ID	CP-ART-03-2022-001250.R1
Article Type:	Paper
Date Submitted by the Author:	09-May-2022
Complete List of Authors:	Curtis, Wyatt; University of Minnesota Twin Cities, Chemical Engineering and Materials Science Willis, Simon; University of Minnesota Twin Cities, Chemical Engineering and Materials Science Flannigan, David; University of Minnesota Twin Cities, Chemical Engineering and Materials Science

SCHOLARONE™
Manuscripts

Single-Photoelectron Collection Efficiency in 4D Ultrafast Electron Microscopy

Wyatt A. Curtis^{1,2}, Simon A. Willis^{1,2}, and David J. Flannigan^{1,2,*}

¹*Department of Chemical Engineering and Materials Science, University of Minnesota, 421*

Washington Avenue SE, Minneapolis, MN 55455, USA

²*Minnesota Institute for Ultrafast Science, University of Minnesota, Minneapolis, MN 55455,*

USA

Abstract: In femtosecond (fs) 4D ultrafast electron microscopy (UEM), a tradeoff is made between photoelectrons per packet and time resolution. One consequence of this can be longer-than-desirable acquisition times for low-density packets, and particularly for low repetition rates when complete photothermal dissipation is required. Thus, gaining an understanding of photoelectron trajectories in the gun region is important for identifying factors that limit collection efficiency (CE; fraction of photoelectrons that enter the illumination system). Here, we continue our work on the systematic study of photoelectron trajectories in the gun region of a Thermo Fisher/FEI Tecnai Femto UEM, focusing specifically on CE in the single-electron regime. Using General Particle Tracer, calculated field maps, and the exact architecture of the Tecnai Femto UEM, we simulated the effects of fs laser parameters and key gun elements on CE. The results indicate CE strongly depends upon the laser spot size on the source, the (unbiased) Wehnelt aperture diameter, and the incident photon energy. The CE dispersion with laser spot size is found to be strongly dependent on aperture diameter, being nearly dispersionless for the largest apertures. A gun crossover is also observed, with the beam-waist position being dependent on the aperture diameter, further illustrating that the Wehnelt aperture acts as a simple, fixed electrostatic lens in UEM mode. This work provides further insights into the operational aspects of fs 4D UEM.

*Corresponding author

Email: flan0076@umn.edu

Office: +1 612-625-3867

1 Introduction

2 Femtosecond (fs) laser-driven pulsed-beam transmission electron microscopy (called 4D
3 ultrafast electron microscopy, UEM) can reach sub-picosecond timescales and has been used to
4 conduct ultrafast pump-probe imaging, diffraction, and element-specific spectroscopy.¹⁻¹¹ For this
5 approach, the pulsed electron beam is typically generated with fs UV pulses and has been
6 successfully extended to all standard gun types used in commercial electron-microscope
7 platforms.^{1,6,12-19} Indeed, it has been shown that both single-shot nanosecond imaging and
8 stroboscopic picosecond imaging can be done *with the identical thermionic electron gun, the same*
9 *cathode, and without the need to adjust the electric fields around the emitter* (base instrument was
10 an FEI Tecnai T12).^{20,21} Properties of the photoelectron packets – and thus the achievable
11 resolutions – can be controlled to some extent with the pulsed laser (*e.g.*, through photon energy,
12 pulse fluence, pulse duration, and laser spot size) and characterized with spectroscopy and cross-
13 correlation methods.^{3,6,8,11,13,15,18,22-27}

14 A key parameter dictating the manner in which materials and phenomena can be studied
15 with UEM is the laser repetition rate (f_{rep}).^{9,13,20,22} Unlike for molecular beams or liquid flow
16 cells, the specimen region in UEM is typically not refreshed prior to arrival of the next
17 photoexcitation pulse. Thus, care must be taken not to induce specimen changes that are
18 temporally long lived compared to f_{rep}^{-1} . That is, one ideally wants the time between packets (f_{rep}^{-1})
19 to be longer than the full specimen recovery time (τ_{rel} ; *e.g.*, electron and lattice thermalization and
20 complete thermal dissipation). This is to avoid creating new long-lived phases or producing
21 irreversible degradation, such as plastic deformation, fracture, or melting. Identifying and using
22 such an f_{rep} – which is material, specimen, and photoexcitation dependent – also enables
23 consistent excitation of the same initial state, such as the ground state.

24 The thin, electron-transparent specimens required for UEM experiments (as with TEM
25 experiments) pose challenges for achieving complete photothermal heat dissipation between
26 excitation pulses for high f_{rep} . However, while operating at the minimum-possible f_{rep} may be
27 preferred for the reasons noted above, beam current is commensurately reduced with lowering f_{rep}
28 (and with all else remaining the same) such that longer acquisition times are needed to reach usable
29 signal levels and contrast strengths. Like with TEM, longer acquisition times can limit resolution
30 due to specimen drift and lab instabilities, system fluctuations, and detector and background signal
31 noise. Beyond creating an extremely stable lab environment, one method for mitigating this is to
32 increase the incident laser pulse fluence and thus the number of photoelectrons per packet for a
33 given f_{rep} . This, however, can lead to deleterious space-charge effects, a reduction in coherence,
34 and thus a reduction in spatiotemporal resolution.^{6,11,22,23}

35 Intuitively, one anticipates optimum beam quality at the lowest-possible acquisition time
36 for a given photon energy ($h\nu$) to be achieved when operating in the so-called single-electron
37 regime, wherein each packet is populated with, on average, one photoelectron.^{1,23,28} In principle,
38 this entirely avoids particle-particle interactions while providing the highest current at a given f_{rep}
39 for a space-charge-free regime. However, this implies that low f_{rep} experiments can be reliably
40 conducted only at low magnifications due to the commensurately long acquisition times and
41 increased blurring due to drift and mechanical/field instabilities. Indeed, high-magnification fs
42 pulsed-beam photoelectron images (*i.e.*, resolved features smaller than 1 nm) have been generated
43 with $f_{rep} \geq 200$ kHz ($f_{rep}^{-1} \leq 5$ μ s) and with acquisition times spanning seconds to minutes.^{2,13,16,19,29}
44 Importantly, however, ultimate quantitative limits of the high-resolution parameter space,
45 particularly for low f_{rep} experiments, have yet to be established for true pump-probe fs UEM
46 imaging (*i.e.*, with specimen photoexcitation); speculative predictions suggest that no better than

47 1 nm will be possible, regardless of f_{rep} .⁶ Though for the predicted photon-induced near-field
48 (*i.e.*, PINEM) aberration, deconvolution of the annular chromatic point spread function should
49 recover the otherwise obscured details.^{3,25,26} As an interesting aside, very few ultrafast pump-
50 probe UEM experiments have been conducted in the weak-excitation regime, where low-fluence
51 pump pulses ($F \sim \mu\text{J}/\text{cm}^2$) induce “dilute” dynamics that are then probed at high f_{rep} common to
52 laser oscillators and beam-blanker pulsers.^{1,20,28,30-38}

53 The main challenges associated with conducting high-resolution UEM (HR-UEM) studies
54 of fs-ps atomic, molecular, and nanoscale materials dynamics seem clear. Accordingly, a path
55 forward involving systematic and increasingly complex modeling and simulations targeted at
56 optimization can be designed.^{23,39} However, the complexity of the instruments and the variety of
57 cathode materials, shapes, and gun types necessitates a thorough, rigorous approach to the
58 development of a quantitative and comprehensive understanding of pulsed-beam behavior in
59 modified commercial instruments.^{13,17,22,40} Indeed, one must contend with particle-particle and
60 particle-field interactions, the precise fields and geometries of all elements comprising the TEM,
61 the properties and behaviors of the laser system, and the unconventional manner in which the TEM
62 is operated when in UEM mode, in addition to lab-specific and laser instabilities.

63 Accordingly, there are significant opportunities to identify and understand the influence of
64 key elements and effects, as well as simple (low-cost) areas of improvement and optimization.^{13,22}
65 In fact, despite fs UEM – defined here as coupling of a fs laser with an otherwise conventional
66 TEM – having been under earnest development and application for nearly 20 years,¹ there is still
67 much to understand about the fundamental behaviors and performance metrics. This is not
68 surprising considering the history of analogous (and still ongoing) efforts dedicated to the more
69 mature methods of ultrafast electron diffraction (UED) and dynamic (nanosecond single-shot)

70 TEM and especially considering the relative simplicity of dedicated UED instruments.^{22,41,42} In
71 fact, one can look to the arc of development of high-resolution TEM, normalized by the associated
72 monetary investment and activity level, to estimate an analogous trajectory for the development of
73 HR-UEM.⁴³⁻⁴⁸

74 Owing to the opportunities noted above, we have initiated an effort to fully and completely
75 characterize and quantify the behavior of single-electron packets in a Thermo Fisher/FEI Tecnai
76 Femto UEM paired with a Light Conversion PHAROS fs pulsed laser, which is the system
77 installed at the University of Minnesota within the Minnesota Institute for Ultrafast Science. One
78 aspect of this effort includes simulating single-electron trajectories for the exact architecture and
79 elements of the Tecnai Femto gun region[†] (*i.e.*, from the electron source to the X-ray aperture)
80 using particle tracing software and calculated field maps. Once complete, we envision modifying
81 and extending these methods to multi-electron packets and to the entire microscope column – from
82 source to detector. We are first focusing on mapping the single-electron regime, which
83 hypothetically should provide the highest resolutions, all else being the same.^{1,6,22,23} Further, it is
84 our hope that the approach and methods we develop, and the insights we glean, can be extended
85 to other systems, thus serving as a useful foundation upon which to build specific descriptions and
86 resolution-focused, operational “phase diagrams” for modality optimization.^{6,13}

87 We have divided our initial effort specific to the electron gun region into three interrelated
88 but conceptually distinct Focus Areas: (1) temporal resolution, (2) collection efficiency (*i.e.*, beam
89 current), and (3) beam coherence. Such a segmented approach allows us to simplify the design of
90 the work, focus our efforts, and compartmentalize the large body of results. We have previously
91 described our findings for single-electron temporal resolution in the gun region (Focus Area 1).³⁹

[†] Provided by Dr. Erik Kieft at Thermo Fisher Scientific.

92 Among other insights, results of the simulations indicate that the statistical electron packet duration
93 can be controlled not only with laser pulse duration and Wehnelt bias,^{6,13} but also with laser spot
94 size, (unbiased) Wehnelt aperture diameter, and incident photon energy (for a fixed work
95 function). This is in addition to the cathode-to-Wehnelt aperture distance.^{13,49}

96 Here, we now focus on simulating and calculating the collection efficiency in the single-
97 electron regime (Focus Area 2). We define collection efficiency (CE) as the fraction of
98 photoemitted electrons that pass through the X-ray aperture and enter the illumination (condenser)
99 system. Accordingly, the CE will range between 0 and 1, with 1 indicating that each photoelectron
100 generated at the source passes through the X-ray aperture. The importance of CE to optimizing
101 UEM beam current and minimizing acquisition time is clear and has been previously noted.^{6,49} As
102 we illustrate here, and as we found in the temporal resolution study, parameters such as laser spot
103 size on the source (and the resulting distribution of transverse momenta), and the Wehnelt-aperture
104 diameter, have a significant impact on the overall behaviors for even the single-electron
105 regime.^{13,39} Indeed, enhanced coupling of single electrons into the illumination system may occur
106 even for an unbiased Wehnelt electrode and an otherwise unmodified TEM, though much
107 additional work is needed, especially for multi-electron packets.^{6,50}

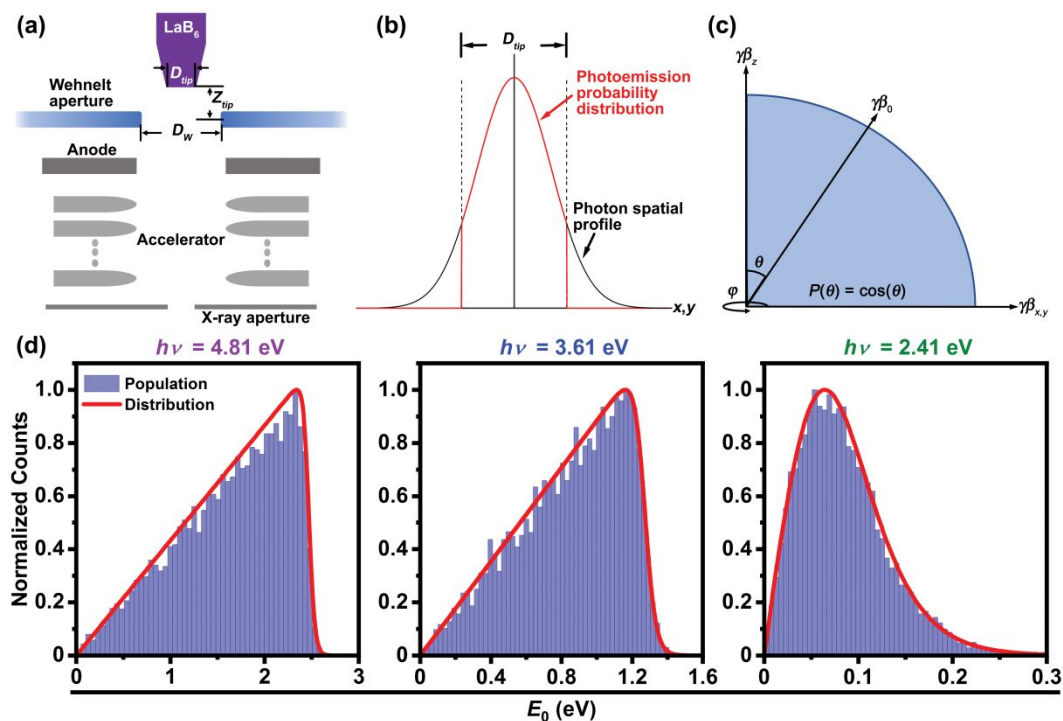
108

109 **Experimental**

110 The elements and dimensions of the Tecnai Femto gun region, as well as the software tools
111 and simulation methods, are the same as those used in the single-electron temporal resolution
112 study.³⁹ Nevertheless, they are again described here for convenience. Particle tracing simulations
113 were conducted using General Particle Tracer (GPT, Pulsar Physics) and cylindrically symmetric
114 field maps calculated with Poisson Superfish.^{51,52} GPT is used to solve the relativistic equations

115 of motion with a fifth-order embedded Runge-Kutta solver and to calculate the Lorentz force acting
 116 on the particle. Poisson Superfish consists of a finite element method used to solve Poisson's
 117 equation for electrostatics. The exact architecture and dimensions for the gun region of the Thermo
 118 Fisher/FEI Tecnai Femto UEM (base instrument is a Tecnai T20 G2) comprised the physical
 119 elements (Fig. 1a). The key parameters of interest in the gun were the Wehnelt aperture diameter
 120 (D_w , varied), the LaB₆ tip diameter (D_{tip} , mainly fixed at 180 μm but varied for one set of
 121 simulations), and the aperture-to-tip distance (Z_{tip} , fixed at 350 μm).⁴⁹ In UEM mode, the Wehnelt
 122 triode is unbiased in the Tecnai Femto and thus acts as a simple, fixed electrostatic lens. Indeed,
 123 this is one motivator for conducting detailed simulations of the Tecnai Femto UEM – we seek to
 124 quantitatively determine the effect of an unbiased Wehnelt triode on photoelectron packet
 125 properties and behaviors.^{6,39,50}

126



127

128 **Fig. 1.** Overview of the simulation elements. (a) Simplified schematic of the Tecnai Femto
129 electron gun with key elements and dimensions labeled (not to scale). (b) Representative
130 photoemission probability distribution for the case where the Gaussian laser spot size (*i.e.*, photon
131 spatial profile) is larger than the LaB₆ tip diameter (D_{tip}). (c) Photoemission probability (P) as a
132 function of emission angle (θ) relative to the optical axis of the electron gun. An emission angle
133 of zero corresponds to a trajectory parallel to the optical axis and a maximum emission probability.
134 γ and β are the Lorentz factor and the normalized relativistic velocity, respectively. Their product
135 is the rest-mass-normalized particle momentum used in GPT. (d) Calculated normalized initial
136 photoelectron kinetic energy (E_0) distributions for $h\nu = 4.81, 3.61,$ and 2.41 eV (left, middle, and
137 right, respectively). Reproduced from Ref. 39 with permission from the PCCP Owner Societies.

138

139 Photoemission spot size is defined as a Gaussian laser spot size (fwhm) on the cathode
140 surface.^{1,39} Here, only photoemission from the flat surface is simulated (Fig. 1b), a configuration
141 that can be achieved experimentally by focusing the laser, by using a LaB₆ (or other material)
142 cathode where D_{tip} is larger than the laser spot size, or by using a cathode with a non-emissive
143 guard ring.^{1,11,13,17} For some simulations, the photoemission spot size was fixed at $50\ \mu\text{m}$, the laser
144 spot sized typically used in the University of Minnesota UEM lab.⁵³ To reduce computation time,
145 and to be consistent with the temporal resolution study, simulations were conducted with $n = 5E4$
146 non-interacting particles generated from the cathode along a Gaussian temporal profile set to be
147 $\tau_{laser} = 300$ fs (fwhm). Thus, each data point is the integrated result of the spatial Gaussian
148 distribution (*i.e.*, the photoemission probability distribution, Fig. 1b) of $5E4$ non-interacting
149 particles. The emitted trajectory probability distribution from the cathode [$P(\theta)$] was set to follow
150 a $\cos(\theta)$ behavior azimuthally integrated over an angle φ (Fig. 1c).^{49,54} Again, we did this in order

151 to remain consistent with the temporal resolution study.³⁹ The nature of the initial distribution will
152 affect the CE, mainly due to interactions of the off-axis photoelectrons with the Wehnelt aperture.
153 Thus, it is important to use a consistent approach despite the $\cos(\theta)$ distribution not being employed
154 universally.⁵⁵⁻⁵⁷

155 Photoelectrons generated at the LaB₆ source are accelerated from initial kinetic energies
156 (E_0) dictated by the incident photon energy ($h\nu$) to 200 keV along the accelerator region before
157 reaching the X-ray aperture (Fig. 1a). Here, the LaB₆ work function was fixed at $\Phi = 2.4$ eV.⁵⁸
158 (Note that Φ for LaB₆ is sensitive to a number of factors – use of a different value here will only
159 lead to a commensurate rescaling of the findings. The specific number used in the simulations is
160 less important than the observed trends.) Thus, different distributions of E_0 will result for the
161 different values of $h\nu > \Phi$ simulated here (Fig. 1d). The distributions were modeled as
162 transmission coefficients for a free electron encountering a step potential, and photoemission was
163 approximated by shifting the Fermi-Dirac distribution by the $h\nu$ energy of the incident photon,
164 following the approach taken by Mogren and Reifenberger for LaB₆.⁵⁹ Note again that because
165 we are presently focused on the gun region, the X-ray aperture is the final limiting element in the
166 simulations. Electron packet populations were collected at a virtual screen positioned 35 cm from
167 the photoemission plane. At this position, all electrons have been fully accelerated, have kinetic
168 energies of 200 keV, and have propagated past the X-ray aperture plane.³⁹

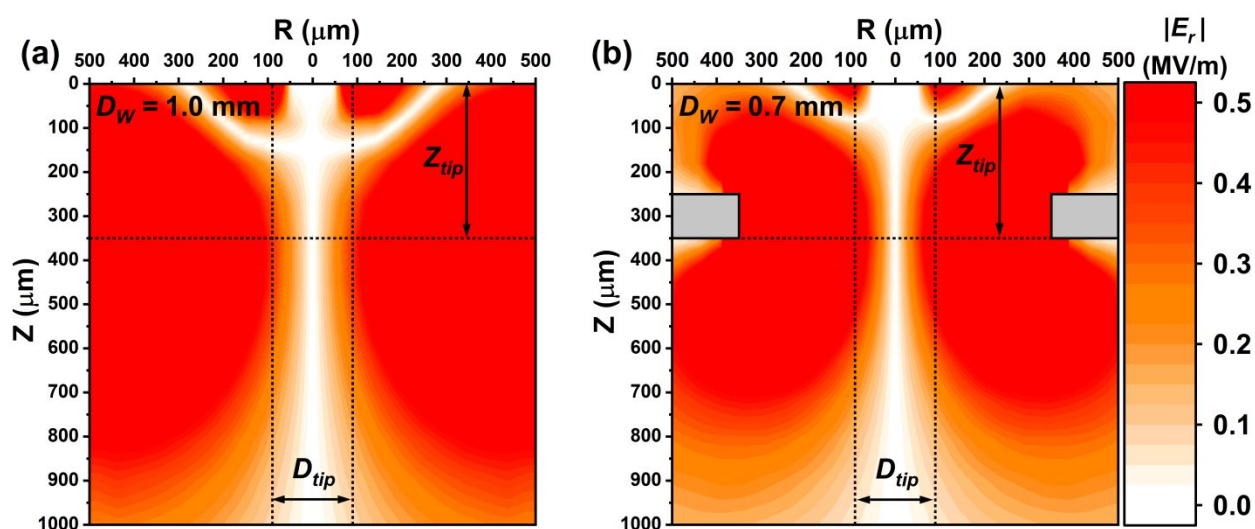
169

170 **Results and discussion**

171 **Unbiased Wehnelt aperture interaction strength.** A key parameter for determining the
172 Wehnelt-aperture lensing behavior is the beam radius in the aperture plane. As described in the
173 Experimental section, the Wehnelt aperture is at zero bias relative to the photoemitter (-200 kV)

174 and thus acts as a weak electrostatic lens in the tip region of the electron gun. Nevertheless, emitted
 175 electrons experience repulsive transverse forces that depend on D_W and the beam radius in the
 176 aperture plane. Figure 2 shows the calculated spatial distributions of the magnitudes of the
 177 transverse electric fields ($|E_r|$) in the tip region of the electron gun for $D_W = 0.7$ and 1.0 mm. As
 178 can be seen, the $D_W = 0.7$ mm aperture generates a field distribution that permeates further into the
 179 footprint of D_{tip} . In addition, the electric-field gradient is steeper within this footprint for the
 180 smaller aperture. Accordingly, off-axis photoelectrons experience a stronger field gradient for
 181 smaller apertures and a given cathode size. Indeed, the difference in transverse displacements of
 182 the electrons is on the order of millimeters for the different aperture diameters (see below).
 183 Further, larger apertures provide a larger field-free region centered on the optical axis, in addition
 184 to generating a more expansive electric field overall – for example, compare the $|E_r|$ values
 185 spanning the 180 μm centered at $R = 0 \mu\text{m}$ for the $Z = 1$ mm positions in Figure 2a,b. No temporal
 186 broadening occurs within this field-free region.³⁹

187



188

189 **Fig. 2.** Electric field contour maps in the vicinity of the unbiased Wehnelt aperture for (a) $D_W =$
 190 1.0 mm and (b) $D_W = 0.7$ mm. The horizontal dotted line at $Z = 350 \mu\text{m}$ marks the position of the

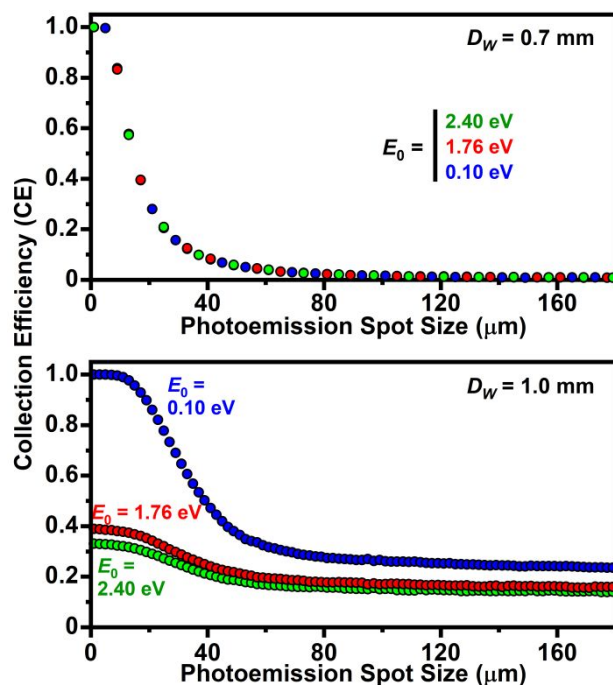
191 outer face of the Wehnelt aperture (relative to the emitter surface at $Z = 0 \mu\text{m}$). This defines the
192 Z_{tip} dimension. The vertical dotted lines mark the edges of the cathode surface and thus define the
193 D_{tip} dimension (180 μm diameter). The color bar displays the scale of the electric-field magnitude,
194 $|E_r|$. The grey rectangles centered at $Z = 300 \mu\text{m}$ in (b) represent the Wehnelt aperture edges,
195 which extend out to $R = 350 \mu\text{m}$; the aperture edges are flush with the vertical borders in (a).

196

197 Two main factors affect beam radius in the Wehnelt aperture plane: (1) the initial emission
198 point relative to the optical axis (*i.e.*, the position relative to $R = 0$), and (2) the initial electron
199 kinetic energy, E_0 . The first factor is a direct modulation of the initial spot size of the electron
200 beam (determined by the laser spot size on the cathode). The second factor can be understood by
201 noting that electrons with higher E_0 have larger transverse momenta, thus leading to a relative
202 increase in the initial integrated packet divergence. The effect these factors have on CE can be
203 illustrated by considering single electrons emitted from $R = 45 \mu\text{m}$ and $R = 90 \mu\text{m}$ with $E_0 = 2.40$
204 eV and with initial trajectories normal to the Wehnelt aperture. For the $D_w = 1.0 \text{ mm}$ aperture, the
205 difference in $|E_r|$ in the aperture plane at these two positions is 0.21 MV/m. Assuming constant
206 Wehnelt interactions and no transverse acceleration by the accelerating field, the calculated
207 difference in transverse displacement is 8 mm after 2 ns of propagation (roughly the gun escape
208 time). This is a significant displacement and indicates the more strongly-deflected electron will
209 not pass through the X-ray aperture (diameter $< 8 \text{ mm}$), thus illustrating the impact on CE. Also
210 note that electrons with higher E_0 have larger longitudinal momenta, on average, which shortens
211 the residence time in the aperture transverse fields leading to a weaker convergence. Having
212 established the general effects of an unbiased Wehnelt electrode, the effects of specific electron-
213 gun elements and laser parameters on CE are now considered.

214 **Dependence of CE on photoemission spot size for key values of D_W .** As was done in
215 the temporal resolution study,³⁹ we first established baseline behaviors for single-electron CE by
216 simulating three key and discrete initial photoelectron kinetic energies ($E_0 = 0.10, 1.76, \text{ and } 2.40$
217 eV) for $D_W = 0.7$ and 1.0 mm. Beginning by using three discrete energies instead of the
218 distributions shown in Figure 1d serves as a first approximation to the more complex but also more
219 realistic cases. As can be seen in Figure 3, a strong dependence of CE on photoemission spot size
220 and D_W is generally observed; CE decreases with increasing spot size for both values of D_W .
221 However, precise behaviors for each of the E_0 values vary and strongly depend upon D_W . First,
222 while the behaviors for each of the E_0 values are identical for $D_W = 0.7$ mm (Fig. 3, top panel), the
223 $E_0 = 0.10$ eV energy deviates significantly from the 1.76 and 2.40 eV energies for $D_W = 1.0$ mm
224 (Fig. 3, bottom panel). Second, while CE = 1.0 for all E_0 at spot sizes below $5 \mu\text{m}$ for $D_W = 0.7$
225 mm, only the 0.10 eV energy shows a CE = 1.0 (for spot sizes below $20 \mu\text{m}$) for the 1.0 mm
226 aperture. The higher E_0 energies attain maximum CE values between 0.33 (2.40 eV) and 0.38
227 (1.76 eV). Third and finally, while CE rapidly decreases to below 0.01 with increasing spot size
228 for all E_0 for $D_W = 0.7$ mm, the lowest value for $D_W = 1.0$ mm is 0.14 for $E_0 = 2.40$ eV.

229



230

231 **Fig. 3.** Single-electron-packet collection efficiency (CE) as a function of photoemission spot size
 232 for three discrete values of E_0 for $D_W = 0.7$ mm (top panel) and 1.0 mm (bottom panel).

233

234 The general behaviors shown in Figure 3 again arise from the Wehnelt aperture acting as a
 235 weak, fixed electrostatic lens when in UEM mode (*i.e.*, absent feedback biasing). As such, the
 236 distance of an electron from the center $x,y = 0,0$ position in the plane of the Wehnelt aperture –
 237 which is determined by the initial photoemission position and momentum – determines the
 238 transverse electric-field strength experienced by the propagating electron. Note that here we are
 239 assuming a perfectly flat LaB₆ emitting surface; initial trajectories from actual cathodes will be
 240 more complex owing to surface roughness, structural and compositional evolution with time, and
 241 adsorption of contaminating species.^{58,60-62} Here, we observe that the divergence of an electron
 242 after the Wehnelt aperture scales with photoemission spot size, which then impacts the integrated
 243 transverse packet radius (parameterized here as the fwhm diameter, D_{packet}) as it is accelerated
 244 toward the X-ray aperture. Accordingly, one would expect a larger fraction of the total population

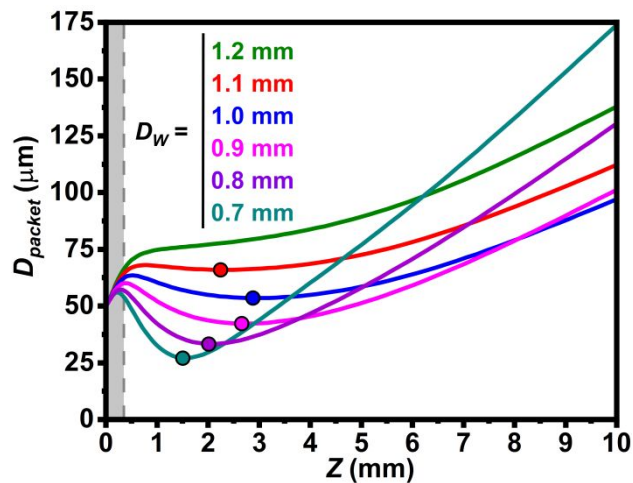
245 exiting the Wehnelt to ultimately be blocked by the X-ray aperture for larger photoemission spot
246 sizes; these electrons will not enter the illumination system, and the CE will be reduced.

247 Overall, the simulation results indicate that both the single-electron CE and the temporal
248 resolution can be improved by reducing the photoemission spot size for a given D_W (*i.e.*, by
249 creating a tighter laser focus on the LaB₆ surface while in the single-electron regime).^{13,39} Possible
250 practical avenues for further reducing the photoemission spot size on the source could involve
251 expansion of the laser spot diameter on the final focusing lens (limited by clipping requirements
252 along the beam path) or redesign of the internal laser path to minimize the distance between the
253 final lens and the photocathode. As an aside, we hypothesize that this also may have implications
254 for the ideal electron source shape for laser-driven UEM.²² Note also that CE values of 1.0 for
255 certain gun configurations have been previously predicted,⁴⁹ which has significant implications for
256 the role of aperturing and reductions in beam current in the condenser system – this is a key area
257 of interest for future work. As shown below, regimes with CE values of 1.0 are also predicted to
258 exist when considering the full E_0 distribution (Fig. 1d), even for $h\nu = 4.81$ eV and $\Phi = 2.4$ eV.
259 However, full system simulations are required to gain insights into the fraction of photoelectrons
260 making it to the specimen and to the detector.

261 **Energy filtering and the presence of a gun crossover.** The difference in CE at a select
262 spot size for discrete E_0 values for $D_W = 1.0$ mm shown in Figure 3 (bottom panel) suggests that a
263 serendipitous energy filtering effect is at work in the gun region. This filtering leads to a narrowing
264 of the electron-energy distribution arising from preferential aperturing of electrons with higher
265 initial kinetic energies, analogous to aperturing the beam further down the column. The potential
266 origins of this effect can be illustrated by analyzing a simulation of the transverse beam properties
267 for a fixed E_0 and a fixed photoemission spot size as electrons exit through Wehnelt apertures of

268 various D_W (Fig. 4). Here, we chose $E_0 = 1.76$ eV and a photoemission spot size of $50 \mu\text{m}$. We
 269 simulated how the packet diameter, D_{packet} , evolves from the LaB_6 surface ($Z = 0$) to a longitudinal
 270 position $Z = 10$ mm for D_W ranging from 0.7 mm to 1.2 mm. Note that all gun elements within
 271 this longitudinal distance were included in the simulation despite not being explicitly shown in the
 272 figure.

273



274

275 **Fig. 4.** Evolution of photoelectron packet diameter (D_{packet}) for a $50 \mu\text{m}$ laser spot size, for $E_0 =$
 276 1.76 eV, and for Wehnelt aperture diameters (D_W) ranging from 0.7 mm to 1.2 mm. The LaB_6
 277 cathode surface is at $Z = 0$, and the grey shaded region denotes the Z_{tip} region (see Fig. 1a). The
 278 dashed grey line is the plane of the Wehnelt aperture. The colored dots mark the beam waists (w_0)
 279 for each aperture size and were found by taking using a first-derivative analysis of the beam
 280 diameter in MATLAB.

281

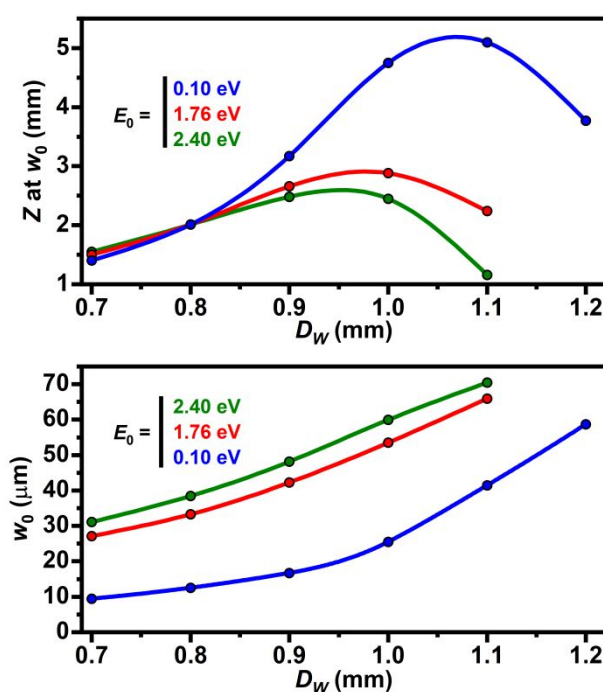
282 Several notable behaviors emerge from the beam dynamics simulations summarized in
 283 Figure 4. First, while D_{packet} initially increases upon moving away from the LaB_6 surface ($Z = 0$),
 284 the smaller diameter apertures show a noticeable decrease in D_{packet} before reaching the aperture

285 plane ($Z = 0.35$ mm; see, for example, $D_W = 0.7$ mm). Second, while D_{packet} appears to be always
286 increasing for $D_W > \sim 0.9$ mm and $Z \leq 0.35$ mm, smaller aperture values show a decrease before
287 reaching the aperture plane. Third, all values of D_{packet} except for the 1.2 mm aperture continue to
288 decrease once past the aperture plane before again increasing. This reduction in D_{packet} once past
289 the aperture results in a beam waist, w_0 , generally positioned within 3 mm of the source surface
290 and increasing in size with increasing D_W . *This is indicative of a crossover and occurs for aperture*
291 *sizes less than 1.2 mm, despite the Wehnelt being unbiased.* Further, the Z position of w_0 (*i.e.*, the
292 crossover point, Z_{w_0}) shows an increase and then decrease in going from 0.7 to 1.1 mm. Fourth,
293 the smaller apertures show stronger divergence to larger D_{packet} for $Z > Z_{w_0}$. Generally, these
294 behaviors are dictated by the resulting proximity and thus the transverse electric field magnitude
295 experienced by the statistical photoelectron packet. Accordingly, reducing the photoemission spot
296 size for a given D_W has the same basic effect as increasing D_W for a given spot size; Z_{w_0} will first
297 increase and then decrease, and the divergence to larger D_{packet} for $Z > Z_{w_0}$ will go down.

298 Having established the behavior of D_{packet} for $Z \leq 10$ mm from the LaB₆ surface for a single
299 initial kinetic energy, we next simulated and compared the beam waist position (*i.e.*, crossover
300 position) and size for all three discrete values of E_0 shown in Figure 3, again for a photoemission
301 spot size of 50 μm . Figure 5 shows a summary of the results for $D_W = 0.7$ to 1.2 mm. Note that
302 no crossover occurs for the specific cases of $E_0 = 1.76$ and 2.40 eV and $D_W = 1.2$ mm. In these
303 cases, D_{packet} continuously expands as it propagates from the cathode surface to $Z = 10$ mm,
304 indicating that interactions with the aperture field are too weak to induce a dramatic change in
305 transverse momentum. While the general behaviors of Z_{w_0} and w_0 are similar for each E_0 , two
306 obvious trends can be seen. First, the increasing and decreasing behavior of Z_{w_0} with increasing
307 D_W , as seen in Figure 4, occurs for each energy, but the maximum value of Z_{w_0} for all simulated

308 apertures increases with decreasing E_0 (Fig. 5, top panel). This shows that, for a given D_W and
 309 photoemission spot size, the crossover point of initially higher energy photoelectrons will be
 310 positioned closer to the Wehnelt aperture – *a range of crossover points will be present for a range*
 311 *of E_0 .* Second, again as seen for $E_0 = 1.76$ eV in Figure 4, w_0 steadily increases with increasing
 312 D_W , with higher kinetic energy photoelectrons generally having larger beam waists for a given
 313 aperture diameter (Fig. 5, bottom panel).

314



315

316 **Fig. 5.** Photoelectron beam waist behavior as a function of Wehnelt aperture size for three discrete
 317 initial kinetic energies. The top panel shows the crossover position (Z_{w_0}) between the cathode
 318 surface and $Z = 10$ mm from the surface, while the bottom panel shows how w_0 varies, both as a
 319 function of D_W for the initial kinetic energies noted. The solid curves are spline interpolations of
 320 the individual points and are included to guide the eye and to show the general trends. Here, w_0
 321 and the crossover position were found using a first-derivative analysis of beam diameter in
 322 MATLAB.

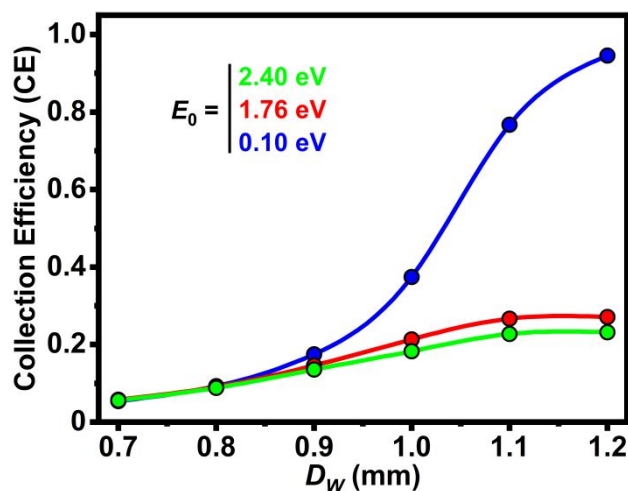
323

324 The behaviors shown in Figure 5 arise from effects of a lower initial deviation of transverse
325 momentum for the lower kinetic energy photoelectrons – the interaction strength with the aperture
326 field can be qualitatively appreciated by noting how the position and size of w_0 for each E_0 shift
327 relative to one another. That is, the resulting crossover properties are entirely contingent upon
328 how the photoelectrons are lensed by the unbiased Wehnelt aperture. While the photoemission
329 spot size is fixed, D_{packet} clearly varies as the photoelectrons are accelerated toward the X-ray
330 aperture (see Fig. 4). For a given E_0 , reduced values of D_W create smaller packet diameters at the
331 aperture plane – this again can be seen by inspecting the $Z = 0.35$ mm position in Figure 4 for E_0
332 $= 1.76$ eV. *As noted above, increasing D_W has the same basic effect as reducing the size of the*
333 *photoelectron beam for a fixed aperture size.* This is because the interaction strengths are reduced
334 due to simple proximity arguments. As illustrated in Figure 5, this is also the case for varying
335 initial kinetic energies – fewer photoelectrons are strongly impacted by electrostatic lensing at
336 lower initial kinetic energies because the initial deviation in transverse momentum is
337 commensurately lower. Note that the increase in slope for each E_0 above $D_W \sim 0.9$ mm is also an
338 indication of how the populations are shifting toward weaker overall interactions, with lower E_0
339 being impacted to a greater degree, as expected (Fig. 5, lower panel).

340 **CE as a function of D_W for a fixed laser spot size.** Having identified the presence of a
341 gun crossover and an energy filtering effect, we next analyzed the simulated trajectories for the
342 entire gun region (*i.e.*, from source to X-ray aperture) in order to determine the behavioral
343 dependence of CE on D_W . The electron-packet parameters were the same as those shown in Figure
344 3. The photoemission spot size was fixed at $50 \mu\text{m}$, while D_W was varied from 0.7 to 1.2 mm. As
345 can be seen in Figure 6, while all three discrete values of E_0 show an increase in CE with increasing

346 D_W , the higher energies reach maximum values of only 0.23 and 0.27 at $D_W = 1.2$ mm ($E_0 = 2.40$
347 and 1.76 eV, respectively). Comparatively, the $E_0 = 0.10$ eV energy reaches a value of 0.95. Note,
348 however, that CE vs. D_W generally shows a sigmoidal response indicating that values of $D_W > 1.2$
349 mm will result in little or no additional increase in CE, regardless of E_0 . Indeed, the higher energies
350 show increases in CE of only $\sim 0.4\%$ in going from $D_W = 1.1$ to 1.2 mm. Conversely, for the
351 smallest diameters simulated (0.7 and 0.8 mm), CE is nearly identical for all values of E_0 ; clear
352 deviations begin to appear for $D_W > 0.8$ mm.

353



354

355 **Fig. 6.** Collection efficiency (CE) as a function of Wehnelt aperture diameter (D_W) for three
356 discrete values of E_0 and a photoemission spot size of 50 μm .

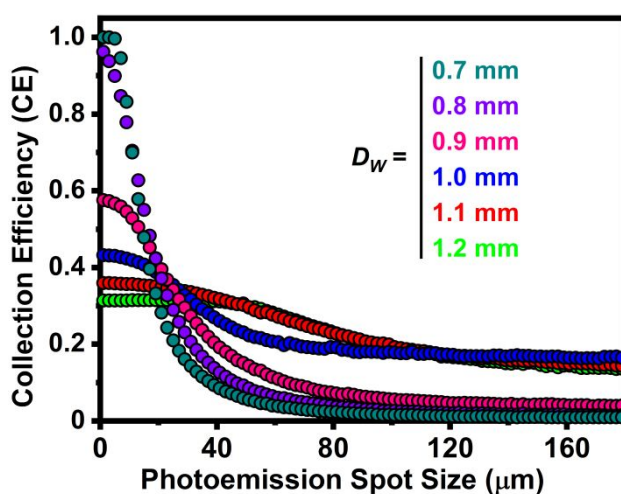
357

358 As with the other simulated behaviors, the trends shown in Figure 6 can be explained by
359 considering the interaction strength between the Wehnelt-aperture field and the photoelectrons.
360 For example, a decreased interaction strength, as occurs for larger aperture sizes (or smaller laser
361 spot sizes) and lower E_0 , results in a larger number of initially off-axis photoelectrons (*i.e.*, those
362 not emitted from the $x,y = 0,0$ LaB₆ center position) passing through the X-ray aperture. This can

363 be understood by recognizing that photoelectrons with lower E_0 values have on average lower
364 transverse velocities, which leads generally to a decrease in interaction strength with the aperture.
365 For the parameter space explored here (*e.g.*, 50 μm spot size), this appears to be true for $D_W > 0.8$
366 mm, where CE becomes dependent on E_0 . One might conclude from this that there is a combined
367 D_W and spot-size threshold value for CE divergence based on E_0 that shifts to smaller aperture
368 sizes for smaller laser spot sizes. Note, however, that the electrostatic field strength in the plane
369 of the Wehnelt aperture becomes increasingly uniform with decreasing D_W (see Figure 2). Thus,
370 using smaller laser spot sizes with small Wehnelt apertures only produces an overall increase in
371 CE, independent of E_0 (see Figure 3). That is, the x,y position of photoemission from the source
372 determines if the photoelectron will be deflected by the Wehnelt-aperture electrostatic field,
373 independent of transverse momentum. Overall, this shows that higher values of CE are found for
374 lower E_0 and for larger D_W , as expected from the results already discussed. As importantly,
375 however, smaller apertures can be used in conjunction with smaller laser spot sizes to generate
376 dramatically improved beam currents and perhaps also improved coherence, potentially at the cost
377 of temporal resolution.³⁹

378 **CE for an $h\nu$ -determined E_0 distribution for $\Phi = 2.4$ eV.** To this point, we have
379 simulated discrete values of E_0 in order to determine baseline behaviors. While useful, behaviors
380 based on the distributions shown in Figure 1d are expected to more accurately reflect experiments.
381 Thus, we repeated the simulations shown in Figure 3 for a range of D_W but this time using the E_0
382 distribution generated with $h\nu = 4.81$ eV, the results of which are summarized in Figure 7. All
383 other parameters were kept the same. As was the case for the discrete values of E_0 , a general
384 decrease in CE was observed with increasing photoemission spot size for all D_W . Further, the
385 effect was weakened for larger D_W , again as generally seen for discrete values of E_0 – the smallest

386 apertures showed the largest CE dispersion behaviors, with the effects being dramatically
 387 decreased with increasing D_W . In addition, CE is very roughly the same (~ 0.33) for all aperture
 388 diameters at a photoemission spot size of $\sim 20 \mu\text{m}$ and, owing to the relative dispersions, is visually
 389 analogous to a spectroscopic isosbestic point. Also, while CE for all D_W tends to become mostly
 390 independent of spot size at values above $\sim 90 \mu\text{m}$, a clear bifurcation occurs between 0.9 and 1.0
 391 mm. That is, above $\sim 90 \mu\text{m}$, CE is ~ 0.15 for $D_W \geq 1.0 \text{ mm}$ but is only ~ 0.02 for $D_W \leq 0.9 \text{ mm}$.
 392



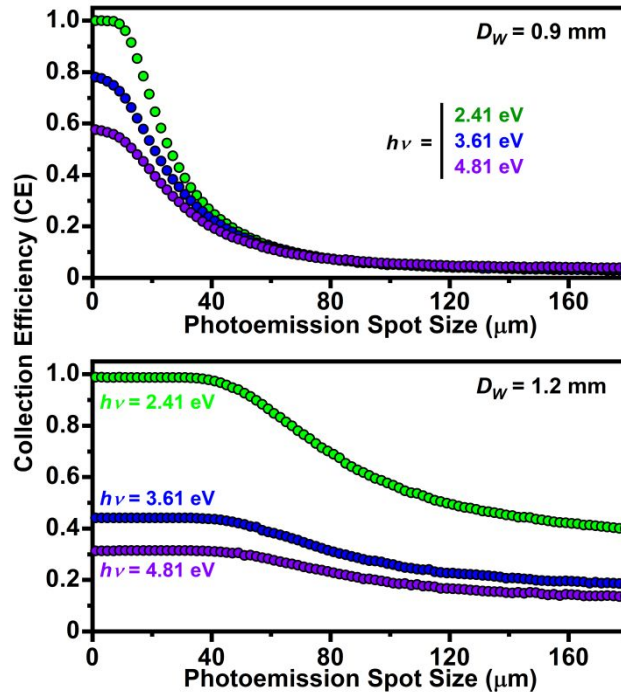
393
 394 **Fig. 7.** Collection efficiency (CE) as a function of photoemission spot size for a range of Wehnelt
 395 aperture diameters (D_W) for the $h\nu = 4.81 \text{ eV } E_0$ distribution (Fig. 1d).

396
 397 The general behaviors shown in Figure 7 again arise from the same interactions that
 398 generated the results shown in Figure 3. Basically, a larger number of photoemission events
 399 occurring far from the $x,y = 0,0$ source center point ultimately leads to a lower CE due to losses at
 400 the X-ray aperture. Further, the results suggest that, for spot sizes between roughly 20 and 100
 401 μm , gains in CE are possible only by using a larger Wehnelt aperture, in essence by decreasing the
 402 interaction strength felt by off-axis photoelectrons. For example, in our lab, we have a $50 \mu\text{m}$ spot

403 size on the electron source (measured externally and then extrapolated to the source),⁵³ we use a
404 1.0 mm diameter aperture, and we routinely use $h\nu = 4.81$ eV photons for photoemission. For
405 these conditions, the simulation results shown in Figure 7 predict a CE of $\sim 20\%$ for the single-
406 electron regime. This could be further improved to $\sim 30\%$ by using a 1.1 mm diameter aperture
407 but with no further improvement for a 1.2 mm aperture. Other ways to improve CE would include
408 using lower energy photons for photoemission, but any gains might be offset by losses arising
409 from the reduced quantum efficiency.

410 **CE for all three $h\nu$ -determined E_0 distributions for select D_W .** For comparison, the
411 specific case for $h\nu = 4.81$ eV shown in Figure 7 was extended to the other two E_0 distributions
412 shown in Figure 1d. Figure 8 displays the results for two key aperture sizes, $D_W = 0.9$ and 1.2
413 mm. We focused on these two diameters because they constitute elements of the bifurcated
414 groupings shown in Figure 7, and they also display significantly different dispersion behaviors
415 with spot size for $h\nu = 4.81$ eV. As with the highest photon energy, the two other E_0 distributions
416 also show a general reduction in CE with increasing spot size for both apertures. The CE
417 dispersion is again more significant for the smaller aperture, with all spot sizes above ~ 60 μm
418 having the same value regardless of $h\nu$ (Fig. 8, top panel). *This suggests that, for this aperture*
419 *size, there is no benefit to using different incident photon energies with respect to CE for spot sizes*
420 *larger than this critical value.* Further, the gains below ~ 60 μm are less than a factor of two,
421 suggesting reductions in beam current due to reduced quantum efficiency may outweigh any such
422 modest gains. Compared to the 0.9 mm aperture, the dispersions for $D_W = 1.2$ mm are less severe,
423 and thus the CE values with increasing spot size are more robust. Indeed, constant values for each
424 of the E_0 distributions are seen for spot sizes up to 40 μm .

425



426

427 **Fig. 8.** Collection efficiency (CE) as a function of photoemission spot size for the E_0 distributions
 428 generated from $h\nu = 2.41, 3.61,$ and 4.81 eV for Wehnelt aperture diameters (D_W) of 0.9 mm (top
 429 panel) and 1.2 mm (bottom panel).

430

431 While reducing the approach into Focus Areas aids systematic study and clear reporting,
 432 practical aspects must ultimately be considered once the overall description takes shape. To a first

433 approximation, the average UEM photoelectron beam current (I_{pe}) is given as $I_{pe} = \left[\left(\frac{E_p}{h\nu} \cdot \eta \right) \cdot CE \right]$

434 $\cdot e \cdot f_{rep}$, where E_p is the laser pulse energy, $h\nu$ is the photon energy, $\eta \equiv \frac{n_{pe}}{n_{hv}}$ is the photocathode

435 quantum efficiency (ratio of photoelectrons emitted to photons absorbed), e is the fundamental
 436 charge, f_{rep} is the laser repetition rate, and CE is the collection efficiency defined above. Thus, one

437 must consider multiple factors when optimizing the system for a particular application (e.g., HR-

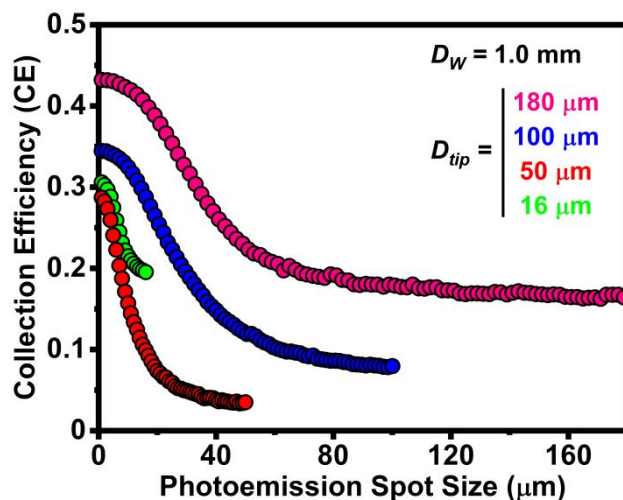
438 UEM). For example, while values of $h\nu$ closer to Φ may give $CE \sim 1$ for $D_W = 1.2$ mm and spot

439 sizes below ~ 40 μm (Fig. 8b) and will also reduce the E_0 spread (Fig. 1d), the large drop in η will

440 more than offset these gains.^{63,64} Therefore, another parameter must be adjusted in order to again
441 increase I_{pe} , likely again at the expense of another beam property. These synergistic effects
442 illustrate the need for a detailed, methodical, and systematic approach, as taken here.

443 **Effect of LaB₆ D_{tip} on CE for $h\nu = 4.81$ eV.** Finally, as seen for the temporal resolution
444 simulations, LaB₆ tip diameter (D_{tip}) was also found to impact CE (Fig. 9).^{13,39} This is due to
445 variations in the pre-Wehnelt-aperture electrostatic fields along the horizontal direction at the tip
446 surface. Four D_{tip} values were simulated for a fixed aperture size of $D_W = 1.0$ mm. While the
447 qualitative behavior is approximately the same for each tip, one can see that CE at a common spot
448 size decreases in going from $D_{tip} = 180$ μm to 50 μm . Interestingly, CE values are approximately
449 the same for the two smallest tip sizes at common spot-size values, indicating the pre-aperture
450 electrostatic fields are minimally impacted with respect to photoelectron divergence and losses at
451 the X-ray aperture. As mentioned above, clearly a balance must be struck between factors such as
452 beam current, temporal resolution, and coherence when considering options and weighing
453 experimental requirements.¹³ For example, while a smaller source size may provide better
454 coherence, one may actually have a better overall beam current with a larger LaB₆ *for a common*
455 *laser spot size*. In our view, insights such as these further emphasize the need to map the available
456 parameter space and develop operational phase diagrams in order to optimize the instrument for a
457 given set of desired conditions – the complexity hinders prediction of some of the more subtle, but
458 nevertheless important, behaviors.

459



460

461 **Fig. 9.** Collection efficiency (CE) as a function of photoemission spot size for $D_W = 1.0$ mm and
 462 the $h\nu = 4.81$ eV E_0 distribution for different D_{tip} values.

463

464 In conclusion, the systematic simulations reported here further add to the operational
 465 phase-space framework for the Tecnai Femto UEM, with the larger body of work potentially
 466 serving as a template for other 4D UEM systems. Because the focus has thus far been on easily
 467 adjustable and interchangeable laser parameters and relatively low-cost microscope elements, we
 468 anticipate being able to identify readily accessible instrument phase space for optimization of
 469 performance, depending upon the measurements of interest (*e.g.*, HR-UEM at low f_{rep} or high f_{rep}
 470 at low specimen excitation). Owing to the systematic approach and quantitative categorization of
 471 conditions and effects performed through simulations, identification and isolation of the effects of
 472 lab and instrument instabilities on the limits of resolution can be more readily determined. Future
 473 work will focus on beam coherence before building in complexity to multi-electron packets and
 474 simulations of the illumination, objective, and projection systems.

475

476 **Author contributions**

477 W. A. C. contributions were data curation, formal analysis, investigation, methodology, software,
478 validation, visualization, writing – original draft, writing – review and editing. S. A. W.
479 contributions were data curation, formal analysis, investigation, methodology, software,
480 validation, visualization, writing – original draft, writing – review and editing. D. J. F.
481 contributions were conceptualization, data curation, funding acquisition, methodology, project
482 administration, resources, supervision, visualization, writing – original draft, writing – review and
483 editing. See the NISO CRediT taxonomy for definitions of contributing roles (credit.niso.org).
484

485 **Conflicts of interest**

486 There are no conflicts to declare.
487

488 **Acknowledgements**

489 This material is based on work supported by the U.S. Department of Energy, Office of Science,
490 Office of Basic Energy Sciences under Award No. DE-SC0018204. This material is based upon
491 work supported by the National Science Foundation Graduate Research Fellowship Program under
492 Grant No. DGE-1839286. This work was supported partially by the National Science Foundation
493 through the University of Minnesota MRSEC under Award Number DMR-2011401.
494 Acknowledgement is made to the Donors of the American Chemical Society Petroleum Research
495 Fund for partial support of this research under Award No. 60584-ND10. We thank Dr. Erik Kieft
496 of Thermo Fisher Scientific for assistance with modeling the FEI Tecnai Femto architecture and
497 for ensuring accurate electrostatic field maps were generated.
498

References

- 499 1. V. A. Lobastov, R. Srinivasan and A. H. Zewail, *Proc. Natl. Acad. Sci. U.S.A.*, 2005, **102**,
500 7069-7073.
- 501 2. H. S. Park, J. S. Baskin, O. H. Kwon and A. H. Zewail, *Nano Lett.*, 2007, **7**, 2545-2551.
- 502 3. B. Barwick, D. J. Flannigan and A. H. Zewail, *Nature*, 2009, **462**, 902-906.
- 503 4. A. H. Zewail, *Science*, 2010, **328**, 187-193.
- 504 5. D. J. Flannigan and A. H. Zewail, *Acc. Chem. Res.*, 2012, **45**, 1828-1839.
- 505 6. L. Piazza, D. J. Masiel, T. LaGrange, B. W. Reed, B. Barwick and F. Carbone, *Chem.*
506 *Phys.*, 2013, **423**, 79-84.
- 507 7. L. Piazza, C. Ma, H. X. Yang, A. Mann, Y. Zhu, J. Q. Li and F. Carbone, *Struct. Dyn.*,
508 2014, **1**, 014501.
- 509 8. D. A. Plemmons, S. T. Park, A. H. Zewail and D. J. Flannigan, *Ultramicroscopy*, 2014,
510 **146**, 97-102.
- 511 9. D. A. Plemmons, P. K. Suri and D. J. Flannigan, *Chem. Mater.*, 2015, **27**, 3178-3192.
- 512 10. R. M. van der Veen, T. J. Penfold and A. H. Zewail, *Struct. Dyn.*, 2015, **2**, 024302.
- 513 11. D. A. Plemmons and D. J. Flannigan, *Chem. Phys. Lett.*, 2017, **683**, 186-192.
- 514 12. H. S. Park, J. S. Baskin, O.-H. Kwon and A. H. Zewail, *Nano Lett.*, 2007, **7**, 2545-2551.
- 515 13. K. Bikker, M. Picher, O. Cregut, T. LaGrange, B. W. Reed, S. T. Park, D. J. Masiel and
516 F. Banhart, *Ultramicroscopy*, 2016, **171**, 8-18.
- 517 14. D. R. Cremons, D. A. Plemmons and D. J. Flannigan, *Nat. Commun.*, 2016, **7**, 11230.
- 518 15. A. Feist, N. Bach, N. Rubiano da Silva, T. Danz, M. Möller, K. E. Priebe, T. Domröse, J.
519 G. Gatzmann, S. Rost, J. Schauss, S. Strauch, R. Bormann, M. Siviš, S. Schäfer and C.
520 Ropers, *Ultramicroscopy*, 2017, **176**, 63-73.
- 521 16. F. Houdellier, G. M. Caruso, S. Weber, M. Kociak and A. Arbouet, *Ultramicroscopy*,
522 2018, **186**, 128-138.
- 523 17. L. Zhang, J. P. Hoogenboom, B. Cook and P. Kruit, *Struct. Dyn.*, 2019, **6**, 051501.
- 524 18. P. K. Olshin, M. Drabbels and U. J. Lorenz, *Struct. Dyn.*, 2020, **7**, 054304.
- 525 19. C. Zhu, D. Zheng, H. Wang, M. Zhang, Z. Li, S. Sun, P. Xu, H. Tian, Z. Li, H. Yang and
526 J. Li, *Ultramicroscopy*, 2020, **209**, 112887.
- 527 20. D. J. Flannigan and A. H. Zewail, *Nano Lett.*, 2010, **10**, 1892-1899.

- 528 21. S. T. Park, D. J. Flannigan and A. H. Zewail, *J. Am. Chem. Soc.*, 2011, **133**, 1730-1733.
- 529 22. M. R. Armstrong, K. Boyden, N. D. Browning, G. H. Campbell, J. D. Colvin, W. J.
530 DeHope, A. M. Frank, D. J. Gibson, F. Hartemann, J. S. Kim, W. E. King, T. B.
531 LaGrange, B. J. Pyke, B. W. Reed, R. M. Shuttlesworth, B. C. Stuart and B. R. Torralva,
532 *Ultramicroscopy*, 2007, **107**, 356-367.
- 533 23. A. Gahlmann, S. T. Park and A. H. Zewail, *Phys. Chem. Chem. Phys.*, 2008, **10**, 2894-
534 2909.
- 535 24. S. T. Park, O.-H. Kwon and A. H. Zewail, *New J. Phys.*, 2012, **14**, 053046.
- 536 25. D. A. Plemmons and D. J. Flannigan, *J. Phys. Chem. A*, 2016, **120**, 3539-3546.
- 537 26. P. K. Olshin, J. M. Voss, M. Drabbels and U. J. Lorenz, *Appl. Phys. Lett.*, 2022, **120**,
538 104103.
- 539 27. C. Gerbig, A. Senftleben, S. Morgenstern, C. Sarpe and T. Baumert, *New J. Phys.*, 2015,
540 **17**, 043050.
- 541 28. M. S. Grinolds, V. A. Lobastov, J. Weissenrieder and A. H. Zewail, *Proc. Natl. Acad.*
542 *Sci. U.S.A.*, 2006, **103**, 18427-18431.
- 543 29. B. Barwick, H. S. Park, O.-H. Kwon, J. S. Baskin and A. H. Zewail, *Science*, 2008, **322**,
544 1227-1231.
- 545 30. G. S. Plows and W. C. Nixon, *J. Phys. E: Sci. Instrum.*, 1968, **1**, 595-600.
- 546 31. A. Gopinath and M. S. Hill, *IEEE Trans. Electron Devices*, 1973, **20**, 610-612.
- 547 32. T. Hosokawa, H. Fujioka and K. Ura, *Rev. Sci. Instrum.*, 1978, **49**, 1293-1299.
- 548 33. V. A. Lobastov, J. Weissenrieder, J. Tang and A. H. Zewail, *Nano Lett.*, 2007, **7**, 2552-
549 2558.
- 550 34. W. Verhoeven, J. F. M. van Rens, E. R. Kieft, P. H. A. Mutsaers and O. J. Luiten,
551 *Ultramicroscopy*, 2018, **188**, 85-89.
- 552 35. I. G. C. Weppelman, R. J. Moerland, J. P. Hoogenboom and P. Kruit, *Ultramicroscopy*,
553 2018, **184**, 8-17.
- 554 36. C. Kisielowski, P. Specht, B. Freitag, E. R. Kieft, W. Verhoeven, J. F. M. van Rens, P.
555 Mutsaers, J. Luiten, S. Rozeveld, J. Kang, A. J. McKenna, P. Nickias and D. F. Yancey,
556 *Adv. Funct. Mater.*, 2019, **29**, 1807818.
- 557 37. J. W. Lau, K. B. Schliep, M. B. Katz, V. J. Gokhale, J. J. Gorman, C. Jing, A. Liu, Y.
558 Zhao, E. Montgomery, H. Choe, W. Rush, A. Kanareykin, X. Fu and Y. Zhu, *Rev. Sci.*
559 *Instrum.*, 2020, **91**, 021301.

- 560 38. S. A. Reisbick, M.-G. Han, C. Liu, Y. Zhao, E. Montgomery, C. Jing, V. J. Gokhale, J. J.
561 Gorman, J. W. Lau and Y. Zhu, *Ultramicroscopy*, 2022, **235**, 113497.
- 562 39. W. A. Curtis and D. J. Flannigan, *Phys. Chem. Chem. Phys.*, 2021, **23**, 23544-23553.
- 563 40. M. Kuwahara, S. Kusunoki, Y. Nambo, K. Saitoh, X. Jin, T. Ujihara, H. Asano, Y.
564 Takeda and N. Tanaka, *Appl. Phys. Lett.*, 2014, **105**, 193101.
- 565 41. W. E. King, G. H. Campbell, A. Frank, B. Reed, J. F. Schmerge, B. J. Siwick, B. C.
566 Stuart and P. M. Weber, *J. Appl. Phys.*, 2005, **97**, 111101.
- 567 42. H. Dömer and O. Bostanjoglo, *Rev. Sci. Instrum.*, 2003, **74**, 4369-4372.
- 568 43. A. V. Crewe, J. Wall and J. Langmore, *Science*, 1970, **168**, 1338-1340.
- 569 44. M. Haider, S. Uhlemann, E. Schwan, H. Rose, B. Kabius and K. Urban, *Nature*, 1998,
570 **392**, 768-769.
- 571 45. P. E. Batson, N. Dellby and O. L. Krivanek, *Nature*, 2002, **418**, 617-620.
- 572 46. P. D. Nellist, M. F. Chisholm, N. Dellby, O. L. Krivanek, M. F. Murfitt, Z. S. Szilagy,
573 A. R. Lupini, A. Borisevich, W. H. Sides and S. J. Pennycook, *Science*, 2004, **305**, 1741.
- 574 47. H. Sawada, F. Hosokawa, T. Kaneyama, T. Ishizawa, M. Terao, M. Kawazoe, T.
575 Sannomiya, T. Tomita, Y. Kondo, T. Tanaka, Y. Oshima, Y. Tanishiro, N. Yamamoto
576 and K. Takayanagi, *Jpn. J. Appl. Phys.*, 2007, **46**, L568-L570.
- 577 48. R. Erni, M. D. Rossell, C. Kisielowski and U. Dahmen, *Phys. Rev. Lett.*, 2009, **102**,
578 096101.
- 579 49. E. Kieft, K. B. Schliep, P. K. Suri and D. J. Flannigan, *Struct. Dyn.*, 2015, **2**, 051101.
- 580 50. B. W. Reed, T. LaGrange, R. M. Shuttlesworth, D. J. Gibson, G. H. Campbell and N. D.
581 Browning, *Rev. Sci. Instrum.*, 2010, **81**, 053706.
- 582 51. K. Halbach and R. F. Holsinger, *Part. Accel.*, 1976, **7**, 213-222.
- 583 52. M. J. De Loos and C. A. J. van der Geer, Proc. 5th Eur. Part. Acc. Conf., Sitges,
584 Barcelona, Spain, 1996.
- 585 53. J. Chen and D. J. Flannigan, *Ultramicroscopy*, 2022, **234**, 113485.
- 586 54. Z. T. Pei and C. N. Berglund, *Jpn. J. Appl. Phys.*, 2002, **41**, L52-L54.
- 587 55. P. Baum, *Chem. Phys.*, 2013, **423**, 55-61.
- 588 56. M. Aidelsburger, F. O. Kirchner, F. Krausz and P. Baum, *Proc. Natl. Acad. Sci. U.S.A.*,
589 2010, **107**, 19714-19719.

- 590 57. C. Weninger and P. Baum, *Ultramicroscopy*, 2012, **113**, 145-151.
- 591 58. H. Ahmed and A. N. Broers, *J. Appl. Phys.*, 1972, **43**, 2185-2192.
- 592 59. S. Mogren and R. Reifengerger, *Surf. Sci.*, 1987, **186**, 232-246.
- 593 60. H. E. Gallagher, *J. Appl. Phys.*, 1969, **40**, 44-51.
- 594 61. A. A. Avdienko and M. D. Malev, *Vacuum*, 1977, **27**, 583-588.
- 595 62. E. K. Storms and B. A. Mueller, *J. Appl. Phys.*, 1979, **50**, 3691-3698.
- 596 63. K. Torgasin, K. Morita, H. Zen, K. Masuda, T. Katsurayama, T. Murata, S. Suphakul, H.
597 Yamashita, T. Nogi, T. Kii, K. Nagasaki and H. Ohgaki, *Phys. Rev. Accel. Beams*, 2017,
598 **20**, 073401.
- 599 64. K. Torgasin, K. Morita, H. Zen, K. Masuda, M. Bakr, K. Nagasaki, T. Kii and H. Ohgaki,
600 *Phys. Scr.*, 2019, **94**, 075701.